MOX-Report No. 40/2021

Computational Fluid-Structure Interaction Study of a new Wave Membrane Blood Pump

Martinolli, M.; Cornat, F.; Vergara, C.

MOX, Dipartimento di Matematica
Politecnico di Milano, Via Bonardi 9 - 20133 Milano (Italy)

mox-dmat@polimi.it http://mox.polimi.it

Computational Fluid-Structure Interaction Study of a new Wave Membrane Blood Pump

M. Martinolli[1], F. Cornat[2], C. Vergara[3]

June 15, 2021

[1] MOX, Dipartimento di Matematica, Politecnico di Milano, Milan, Italy
marco.martinolli@polimi.it

[2] CorWave SA, Clichy, France
francois.cornat@corwave.com

[3] LABS, Dipartimento di Chimica, Materiali e Ingegneria Chimica "Giulio Natta"
Politecnico di Milano, Italy
christian.vergara@polimi.it

Keywords: Left Ventricular Assist Device, Wave membrane blood pump, Fluid-Structure Interaction simulation, Contact model, Parametric analysis, Hemocompatibility

Abstract

Purpose: Wave Membrane Blood Pumps (WMBP) are novel pump designs in which blood is propelled by means of wave propagation by an undulating membrane. In this paper, we computationally studied the performance of a new WMBP design (J-shaped) for different working conditions, in view of potential applications in human patients.
Methods: Fluid-Structure Interaction (FSI) simulations were conducted in 3D pump geometries and numerically discretized by means of the Extended Finite Element Method (XFEM). A contact model was introduced to capture membrane-wall collisions in the pump head. Mean flow rate and membrane envelope were determined to evaluate hydraulic performance. A preliminary hemocompatibility analysis was performed via calculation of fluid shear stress.
Results: Numerical results, validated against in-vitro experimental data, showed that the hydraulic output increases when either the frequency or the amplitude of membrane oscillations were higher, with limited increase in the fluid stresses, suggesting good hemocompatility properties. Also, we showed better performance in terms of hydraulic power with respect to a

previous design of the pump. We finally studied an operating point which achieves physiologic flow rate target at diastolic head pressure of 80 mmHg. **Conclusion**: A new design of WMBP was computationally studied. The proposed FSI model with contact was employed to predict the new pump hydraulic performance and it could help to properly select an operating point for the upcoming first-in-human trials.

1 Introduction

As the prevalence of heart failure continues to rise over time with aging of the population [36], *Left Ventricular Assist Devices* (LVADs) are life-sustaining therapeutic options that offer mechanical circulatory support in end-stage patients [2]. In particular, LVADs could act as a temporary bridge to heart transplantation [5] or as a destination therapy in patients that are not eligible for transplantation [3, 34]. LVADs have to meet many requirements in terms of device implantability [10, 13, 22], durability [14, 38], hydraulic power [19, 26] and hemocompatibility [6, 28]. All currently available LVADs are *rotary blood pumps*. They are small and reliable devices equipped with an internal impeller, which propels blood by rotating at elevated velocities, exerting high stresses on blood cells [16, 33].

A new frontier in the LVAD applications is represented by the *Wave Membrane Blood Pumps* (WMBPs), developed at CorWave SA [11]. In this innovative pump model, blood propulsion is induced by the undulations of an immersed elastic membrane [30]. This wave propagation technology has the potential to pump blood at low stress conditions and consequently with a reduced risk of hemocompatibily-related adverse events. In addition, the pump hydraulic output of WMBPs can be regulated by manipulating the membrane wave frequency and amplitude, potentially adapting to patient specific demands, possibly mimicking the pulsatility of the native heart [11].

In [24], a computational work aimed at studying WMBP performance was performed, based on the numerical solution of the Fluid-Structure Interaction (FSI) problem arising between blood and wave membrane. The developed numerical model was employed to perform three-dimensional simulations of the pump system at different pressure conditions and the results were validated against *in vitro* measurements.

In this study we aimed at taking further steps in the computational analysis of WMBPs, in the direction of the clinical application of the device. First, we examined a revised geometry design of the WMBP (J-shaped), that differs from that studied in [24] primarily in the shape of the membrane, demonstrating improved performance in experimental testing, both in terms of hydraulic power and hemocompatibility. On the modeling side, a contact model [12] was added to study the membrane deformation at high oscillations, which may potentially lead to contact of the membrane with the pump housing. Finally, we provided a preliminary investigation of the potential hematologic impact of WMBPs, study-

ing the distribution of the blood shear stress in the device [4, 29], and identifying non-physiological flow patterns, such as recirculation regions [9, 27].

2 Material and Methods

2.0.1 Wave Membrane Blood Pumps

The aim of LVADs is to reduce the work load of the left ventricle of failed hearts by taking over the blood pumping function. Thus, the wave membrane technology in WMBPs should overcome the pressure difference between the left ventricle (inlet) and the aorta (outlet) to pump the oxygenated blood into the circulatory system.

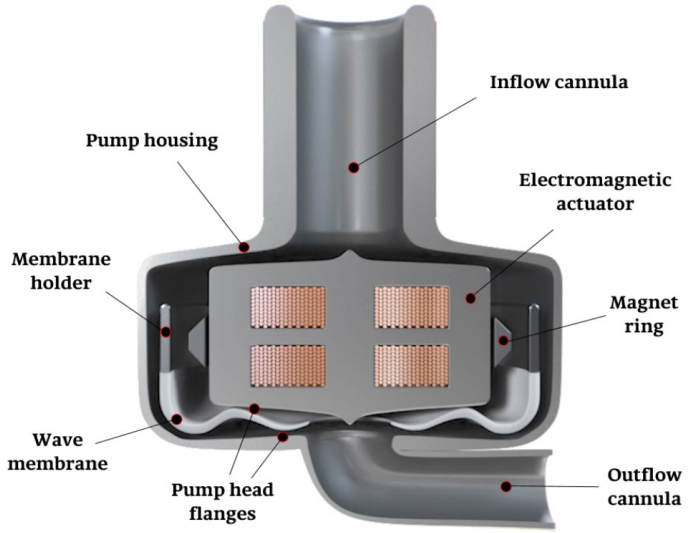

Figure 1: Cross-sectional view of the main components of the implantable wave membrane blood pump, including inlet and outlet channel, the actuator assembly (stator, electromagnetic coils and magnet ring) and the membrane assembly (wave membrane and membrane holder).

The structure of WMBPs comprises the following components (see Figure 1):

- an inflow cannula, implanted at the apex of the left ventricle;
- an outflow cannula, placed at the opposite side of the device and in fluid communication with the ascending aorta via an outflow graft;
- an actuator system, located at the center of the pump chamber, composed of a stator, equipped with two levels of electromagnetic coils, and of a mobile *magnet ring*;

- a membrane assembly, that is suspended within the flow channel, displaced concentrically along the pump longitudinal axis; it includes a rigid *membrane holder*, which is directly connected with the magnet ring, and an elastomeric *wave membrane*, suspended in the so-called *pump head*, *i.e.,* the region delimited by the *pump head flanges*.

The membrane design has been revised to improve pump efficiency and reduce the potential for blood trauma. In this paper we specifically considered two different pump geometries, showed in Figure 2.

In the first pump design (A), extensively studied from a computational point of view in [24], the membrane assembly shows a planar discoidal geometry with an annular membrane holder running along the external edge of the membrane disc (Figure 2, left). Hence, we refer to it as *flat membrane pump design* (or, concisely, *flat design*).

The new pump geometry (B) shows a longer membrane holder that bends towards the inlet up to the magnetic ring (see Figure 2, right). This design is called *J-shape membrane pump design* (or *J-shape design*), due to the shape of the cross-section of the membrane assembly. The additional vertical portion of the membrane holder should work as a flow separator, distributing blood flow across the lower and upper sides of the membrane, and increasing the resistance to antegrade flow to improve hydrodynamic output. Thus, the J-shape design should reduce flow recirculation around the edges of the membrane holder and the exposure time to high shear rates. Other differences with respect to design (A) involve the wider clearance gap between the magnet and the actuator, to reduce local wall shear stress, and the smoother geometry of the housing and of the ring.

WMBPs are activated by an alternating current applied to the electromagnetic coils of the actuator, resulting in an oscillatory motion of the magnet ring and in a deformation wave propagating along the elastic membrane, which is damped by the effect of the surrounding viscous fluid. This results in an energy transfer from the membrane to the blood that ends up in pressure buildup in the flow channel, allowing blood to be pushed towards the outlet channel. Notice that the membrane approaches very closely to the pump flanges (see Figure 1), isolating fluid portions in the flow channel, termed *fluid pockets*, and avoiding potential backflows.

2.1 Experimental Setup

Experimental *in-vitro* data of the hydraulic performance of WMBP were collected in a re-circulating fluid loop, where the response of the system to different hydraulic conditions is measured for any operating point of the membrane. The pump characterization bench consists of a system of reservoir and tubing in which the hydraulic resistance can be modified by centrifugal pumps placed in a series circuit with the WMBP. A glycerin-water solution at 39% concentration

in volume (37 ℃) was used to mimic blood. HQ curves (H: head pressure, Q: flow rate) combine the measurements of the head pressure and the corresponding flow at the outlet, measured with a pressure sensor (PendoTECH, France) and an ultrasonic flowmeter (Sonotec, Germany), respectively. The membrane was equipped with a sensorless position control system that makes the oscillation amplitude closer to a sine function via a feedback loop based on the actuator current [32].

2.2 Mathematical Formulation

The dynamics in WMBP were described by means of an FSI problem with contact, solved in the domain represented in Figure 3.

For the fluid problem, we assumed the blood to be an incompressible, Newtonian and viscous fluid [24, 31] with density ρ_f and viscosity μ_f, and the incompressible Navier-Stokes equations were considered in the fluid domain Ω^f. The latter changes in time due to the movement of the structures formed by two distinct bodies: the membrane assembly Ω^m and the magnet ring Ω^r. Following [24], we assumed the membrane made of a homogenous and isotropic material with density ρ_m, whose deformation is described by a linear infinitesimal elasticity model, with Lamé parameters λ_m and μ_m. On the contrary, the magnetic ring Ω^r was modeled as a rigid structure, whose vertical movement has an impact on determining the fluid domain.

The fluid and structure problems were coupled at the interface Σ to guarantee geometric consistency and physical continuity of velocities and tractions. Accordingly, the FSI problem reads as follows: for each time $t \in (0, T]$, find the fluid velocity $\mathbf{u}$, the fluid pressure p, and the structure displacement $\widehat{\mathbf{d}}$, such that:

$$
\begin{aligned}
\rho_f \left(\partial_t \mathbf{u} + \mathbf{u} \cdot \nabla \mathbf{u}\right) - \nabla \cdot \mathbf{T}^f(\mathbf{u}, p) &= \mathbf{0} && \text{in } \Omega^f(\mathbf{d}), \\
\nabla \cdot \mathbf{u} &= 0 && \text{in } \Omega^f(\mathbf{d}), \\
\rho_m \partial_{tt} \widehat{\mathbf{d}} - \widehat{\nabla} \cdot \widehat{\mathbf{T}}^s(\widehat{\mathbf{d}}) &= \mathbf{0} && \text{in } \widehat{\Omega}^s, \\
\mathbf{u} &= \partial_t \mathbf{d} && \text{on } \Sigma(\mathbf{d}), \\
\mathbf{T}^f(\mathbf{u}, p)\, \mathbf{n} - \mathbf{T}^s(\mathbf{d})\, \mathbf{n} &= \chi \mathbf{n}_w && \text{on } \Sigma(\mathbf{d}),
\end{aligned}
\tag{1a}
$$

where $\widehat{\mathbf{T}}^s(\widehat{\mathbf{d}}) = \lambda_m \left(\widehat{\nabla} \cdot \widehat{\mathbf{d}}\right) \mathbf{I} + 2\mu_m \widehat{\mathbf{D}}(\widehat{\mathbf{d}})$ is first Piola-Kirchhoff structure tensor, coinciding with the Cauchy one due to the small displacement regime, and $\mathbf{T}^f(\mathbf{u}, p) = -p\mathbf{I} + 2\mu_f \mathbf{D}(\mathbf{u})$, with $\mathbf{D}(\mathbf{u}) = \frac{1}{2}(\nabla \mathbf{u} + \nabla \mathbf{u}^T)$, is the fluid Cauchy stress tensor. Quantities with $\widehat{\ }$ refer to a Lagrangian framework, the other ones to an Eulerian framework. We have also highlighted the dependence of the fluid domain Ω^f on the structure displacement $\mathbf{d}$ (*geometric coupling*) and indicated by $\mathbf{n}$ the external fluid normal.

Notice that in the continuity of traction (1a) we added a term χ which modeled a repulsive contact force, acting in the direction of the wall normal $\mathbf{n}_w$, to

describe possible contact between the wave membrane and the pump flanges. Specifically, we considered the *relaxed contact model* [12], that is based on the assumption of an infinitesimal layer of fluid that always separates the fluid-structure interface from the wall boundary. Therefore, we consider a *contact layer* of width ε_c, which extends inwards from the wall boundary. In this framework, when the membrane penetrates into the contact layer, a contact force is applied in the opposite direction to prevent collision and it is assumed to be proportional to the degree of penetration of the structure in the contact layer. In particular, given the distance $g(\mathbf{x})$ between a membrane point $\mathbf{x}$ and the pump wall, we have

$$\chi(\mathbf{x}) = \begin{cases} \dfrac{\gamma_c \mu_m}{h} \left(\varepsilon_c - g(\mathbf{x})\right) & \text{if} \quad g(\mathbf{x}) < \varepsilon_c, \\ 0 & \text{if} \quad g(\mathbf{x}) \geq \varepsilon_c, \end{cases} \tag{2}$$

where γ_c is a positive constant and h is the local mesh size of the fluid mesh, see Figure 4.

In conclusion, we need to prescribe proper initial and boundary conditions. For the latter, we have:

- the head pressure ΔP between the pump outlet Γ^{out} and inlet Γ^{in}, indicating the hydraulic resistance over the pump;
- a sinusoidal displacement with frequency f and amplitude $\phi/2$ (with ϕ being the oscillation *stroke*) on Γ^m and Γ^r, corresponding to the boundaries of the rigid complex formed by the membrane holder and the magnetic ring;
- no-slip wall condition at the boundary Γ^w, indicating the internal pump housing and the stator boundary.

2.3 Hemocompatibility

Hemodynamic quantities were derived from the FSI results to give a preliminary insight on the hemocompatibility of WMBPs. Specifically, we computed a scalar index of the blood shear stress, σ^{scalar}, based on the shear stress tensor $\boldsymbol{\sigma} = \mu_f \mathbf{D}(\mathbf{u})$, used to provide indications about the risk of blood damage in the pump, as done in [6, 23]. In this work, it is defined as

$$\sigma^{scalar} = \sqrt{\frac{1}{6} \sum_{i=1}^{3} \sum_{j=i+1}^{3} (\sigma_{ii} - \sigma_{jj})^2 + \sum_{i=1}^{3} \sum_{j=i+1}^{3} (\sigma_{ij})^2}, \tag{3}$$

in analogy with the Von Mises criterion for blood cells [8]. In particular, the volumetric distribution of σ^{scalar} was investigated to identify potential critical regions in the pump domain. Moreover, the blood *shear rate* field and, in particular, its maximum in space and time value γ^{max} were calculated to compare the risk of shear-induced blood trauma in the J-shape pump design with respect to the results in the flat design presented in [24].

2.4 Numerical Methods

For the numerical solution of the FSI problem we employed the *Extended Finite Element Method* (XFEM) [20], successfully used for several FSI problems with immersed structures [1, 17, 25]. In particular, we specifically referred to the numerical approach proposed in [39] and applied to WMPB in [24], in which a Discontinuous Galerkin (DG) mortaring was employed to weakly couple the fluid and the solid subproblems at the interface. The XFEM-DG technique is an unstructured mesh method using a fixed background mesh with an imposed moving immersed structure mesh which cuts the fluid mesh generating general polygonal elements. The numerical solution on such cut elements is built by employing the standard basis functions defined on the uncut elements and doubling the degrees of freedom [1, 20]. For this reason, it is particularly suitable for the problem at hand preventing large distortion of the fluid elements in the pump head. For details on the complete discretized problem, we refer the reader to [24].

The novelty with respect to [24] is the integration of the contact model, see (1a)-(2). XFEM framework allowed to easily integrate such a model in the corresponding weak formulation, see [12].

The problem was implemented in the C++ finite element LIFEV library [7] in a multi-thread parallel environment. The linear system has been solved using a generalized minimal residual method (GMRES), with a block Gauss-Seidel preconditioner. In particular, we employed 7 cores (Intel Xeon E5-4610 v2) with 2.3 GHz frequency and a RAM of 252 GB.

2.5 Geometric Aspects

Exploiting the symmetry of the pump, for the numerical experiments we considered a reduced geometry of the pump system, restricted to a 120-degree section (see Figure 5, left), in order to reduce the computational costs.

The construction of the reduced geometry introduces the artificial *cut surfaces* Γ^f_{cut}, Γ^m_{cut} and Γ^r_{cut} on the fluid, membrane, and ring domains, where we prescribed null normal component of the unknown and null tangential stresses.

Starting from CAD geometry files, unfitted meshes were generated using GMESH [18], see Figure 5: a fluid mesh (520k elements), a membrane mesh (400k elements) and a magnet ring mesh (140k elements). In all cases, meshes were locally refined in regions of interest for the pump dynamics, such as the pump head, or with high curvature. Such meshes showed positive convergence results with respect to flow and pressure solutions computed on further refined meshes. Specifically, mesh convergence was studied across four different grids with decreasing mesh size h. The refinement ratio $r_i = {}^{h_{i-1}}/_{h_i}$ (h_i being a representative fluid mesh discretization parameter for the $i-th$ mesh) was computed for each grid i. The indices used for the convergence analysis were the time-averaged flow rate Q at the outlet and the mean pressure $p^{\tilde{\mathbf{x}}}$ at point $\tilde{\mathbf{x}} = [0.0, 0.0, 1.4]$. Ta-

ble 1 reports the values of such quantities and the corresponding approximated relative differences.

Mesh Index	N_i	r_i	Q_i $[l/min]$	e_i^Q	$p_i^{\tilde{\mathbf{x}}}$ $[mmHg]$	e_i^p
1	323k	·	1.24	·	121.50	·
2	440k	1.17	3.33	0.627	122.76	0.021
3	520k	1.05	3.09	0.077	123.09	0.005
4	700k	1.11	3.15	0.019	122.95	0.002

Table 1: Mesh sensitivity analysis. N_i and r_i are the number of fluid mesh tetrahedra and the refinement ratio, respectively. The values of convergence indices $\phi = \{Q_i, p_i^{\mathbf{x}}\}$ are presented for each mesh i, together with the corresponding approximated relative difference $e_i^\phi = |\phi_i - \phi_{i-1}|/|\phi_i|$. Level 3 was selected for the rest of the paper since both e_4^Q and e_4^p are less than 2%.

3 Results

In WMBPs the operating conditions of the device are defined by the following parameters:

a) the head pressure ΔP between the outlet and the inlet ports;

b) the frequency f of membrane oscillation;

c) the oscillation stroke Φ, corresponding to twice the amplitude of the membrane vibration.

In particular, we want to:

1. compare the J-shape membrane pump design (Design B) performance with that of the planar membrane (Design A), see Figure 2 (Sect. 3.1);
2. illustrate the effect of the contact model (see Sect. 2.4) in the numerical results (Sect. 3.2)
3. perform a parametric analysis to study the sensitivity of the solution on each operating parameter (Sect. 3.3);
4. assess preliminary indications about hemocompatibility properties of the pump (Sect. 3.4);
5. study of a new operating point at diastolic head pressure (*nominal operating conditions*), in view of potential WMBP application in human patients (Sect. 3.5).

In all the simulations, the fluid parameters were $\rho_f = 1050$ Kg/m^3 and $\mu_f = 0.0035$ $Pa\,s$, whereas, unless differently specified, the contact parameters were $\varepsilon_c = 0.1$ mm and $\gamma_c = 0.04$.

3.1 Design comparison

We considered the same operational conditions used in [24] for the planar membrane (Design A), detailed in Table 2. In this case, the oscillation parameters were fixed and we just varied the head pressure. We refer to this set of operating points as High-Frequency (HF) points, where $f = 120$ Hz. The pump system was simulated for $T = 0.025$ s, corresponding to three periods of oscillation, using a fixed timestep $\Delta t = 0.0002$ s. The elasticity parameters were $\rho_m = 1125$ $^{Kg}/_{m^3}$, $\lambda_m = 2772\ MPa$ and $\mu_m = 56.6\ MPa$.

OP	**Head pressure** (ΔP)	**Frequency** (f)	**Stroke** (Φ)
HF1	50 mmHg	120 Hz	1.06 mm
HF2	60 mmHg	120 Hz	1.06 mm

Table 2: List of High-Frequency (HF) operating points for design comparison.

In Figure 6 we report, at the instant of maximum membrane oscillation, the results for the operating point HF1 ($\Delta P = 50$ mmHg), in terms of velocity, pressure, and shear rate fields. From these results, we observe physiological values for all the quantities, in particular a favorable pressure gradient generated by the membrane undulations between the pump flanges and the outlet, that overcomes the adverse pressure gradient between inlet and outlet. Moreover, we notice that there are no recirculation areas nearby the edges of the the membrane holder. Indeed, the flow coming from the inner vein of the membrane (region A) is drawn into the outer vein (region B) following the direction of the pressure gradient. The vortex located in the outlet channel (region C) is continuously disturbed at high velocities, thus prohibiting the local formation of thrombus.

Also, we observe that the maximum shear rate γ^{max} is equal to 17156 s^{-1}, in proximity to the membrane tip, while the volumetric mean value at the same time instant is 369.52 s^{-1}. Both these values are significantly lower than proposed critical thresholds (e.g. $42000\, s^{-1}$ for hemolysis [4, 6]) confirming what was found for Design A in [24].

In Table 3 we compared the hydraulic performance of the flat design (Design A), taken from [24], and of the J-shape design (Design B), considered in this work. In particular, we computed the outlet flow rate Q and the hydraulic power $W = Q\Delta P$. From these results we can observe the improved hydraulic outputs featured by Design B, in terms of both outflow rate and generated power.

3.2 Analysis of the contact model

The contact model described in Section 2.4 was introduced to capture possible contact dynamics between the wave membrane and the pump head flanges at high oscillations. Indeed, if the membrane deformation is particularly high (for instance at operating points with high stroke), the wave membrane may exit from the pump domain if no contact model is considered (see Figure 7A). This

Head pressure	Design A	Design B
$\Delta P = 50$ mmHg	$Q = 1.792$ $^{L}/_{min}$ $W = 0.19$ W	$Q = 3.62$ $^{L}/_{min}$ $W = 0.40$ W
$\Delta P = 60$ mmHg	$Q = 0.400$ $^{L}/_{min}$ $W = 0.05$ W	$Q = 2.62$ $^{L}/_{min}$ $W = 0.35$ W

Table 3: Estimated time-averaged flow rate at the pump outlet (Q) and hydraulic power (W) for flat pump design (Design A) and J-shape design (Design B) for different pressure conditions. Results for Design A are taken from [24].

results in a non-physical configuration that causes a sudden drop in the flow rate at the outlet. Instead, in presence of the contact model, the repulsive contact force χ, defined in (2), is activated, prohibiting the membrane from exiting the fluid domain and penetrating into the wall (see Figure 7B).

The effectiveness of the contact model depends on two parameters: the thickness of the contact layer ε_c and the penalty constant γ_c, see (2). If ε_c is too narrow or if γ_c is too low, the contact force enabled in the contact layer cannot push the membrane away, obtaining a result very similar to that reported in Figure 7A. At the same time, too high values of ε_c and γ_c should be avoided as well, because the contact model may interfere with the natural wave propagation of the membrane deformation. In our simulations, we used $\varepsilon_c \in [0.05, 0.2]$ mm and $\gamma_c \in [0.02, 0.2]$, depending on the magnitude of the oscillation parameters. Parameter values in these ranges allowed proper representation of the contact dynamics, with a variability in the mean flow at the pump outlet below 5%.

3.3 Parametric analysis

In this section, we report the results obtained for different operating points (OPs) of WMBPs, set by changing the head pressure (P-analysis), the frequency (F-analysis), and the stroke (S-analysis), see Table 4. Notice that the oscillation parameters shifted to lower frequencies and higher strokes than what was observed in Sect. 3.1 (see Table 2), because an increased hydraulic performance was found in this range for the J-shape design. We fixed the timestep Δt to 0.0004 s, so that we obtain 40 to 60 time points per cycle of oscillation for each tested frequency. The values of the membrane parameters ρ_m, λ_m and μ_m are based on the material properties of the membrane. The specific values can be obtained from the membrane material suppliers, but can vary from lot to lot[1].

In Figure 8 we reported the time evolution of the outlet flow rate Q in the P-analysis (left). As expected, Q decreases when ΔP increases, in accordance with the pump functioning. Specifically, the time-averaged outputs amounts to 3.45 $^{L}/_{min}$ at $\Delta P = 50$ mmHg (P1) and to 2.66 $^{L}/_{min}$ at $\Delta P = 60$ mmHg

[1]The reader can contact the authors to ask for access to protected information on membrane dimensions and properties.

OP	**Head pressure** (ΔP)	**Frequency** (f)	**Stroke** (Φ)
P1	50 mmHg	44 Hz	1.5 mm
P2	60 mmHg	44 Hz	1.5 mm
F1	60 mmHg	44 Hz	1.5 mm
F2	60 mmHg	50 Hz	1.5 mm
F3	60 mmHg	60 Hz	1.5 mm
S1	60 mmHg	50 Hz	1.5 mm
S2	60 mmHg	50 Hz	1.6 mm
S3	60 mmHg	50 Hz	1.7 mm

Table 4: List of operating points for the parametric analysis. We grouped them (possibly with overlaps) in three distinct sets: P where ΔP is changed; F where f is changed; S where Φ is changed.

(P2). In the same figure, we also reported a comparison between the computed mean flow value and corresponding experimental *in-vitro* data (right), obtained as described in Sect. 2.1, providing a preliminary result about the validation of our model.

Analogously, in Figure 9, we reported Q for F- and S-analyses. These results show that the output increases when either one of the two parameters increases. Specifically, we have that the averaged-in-time flow rate increases from 2.66 $^{L}/_{min}$ for $f = 44$ Hz (F1), to 3.09 $^{L}/_{min}$ for $f = 50$ Hz (F2) and further to 4.03 $^{L}/_{min}$ for $f = 60$ Hz (F3). Similarly, the averaged-in-time flow rate amounts to 3.09 $^{L}/_{min}$ for $\Phi = 1.5$ mm (S1), to 3.76 $^{L}/_{min}$ for $\Phi = 1.6$ mm (S2) and to 4.39 $^{L}/_{min}$ for $\Phi = 1.7$ mm (S3).

The membrane deformation was studied for different oscillation parameters by looking at the *membrane envelopes*, obtained by reducing the membrane cross-section to its centerline (see Figure 3, right,) and plotting its displacement during one cycle of oscillation. Membrane envelopes can provide important insight in terms of wave propagation and formation of fluid pockets, by analyzing its distance from the pump flange. In Figure 10, we reported the membrane envelopes for operating points F1, F3, S1, S3 (see Table 4). The black lines indicate the relative position of the pump head superior and inferior flanges, with respect to the superior and inferior edges of the membrane, respectively.

Notice that the distance of the membrane envelopes from the pump flanges decreases when f and Φ are higher (F3 and S3), especially with respect to the lower flange, indicating that the fluid pockets are better isolated during their propagation towards the outlet, thus limiting backflows. In addition, in all cases the amplitude of the membrane undulations increases while moving towards the center of the pump (decreasing ξ values), probably as a result of the decreasing thickness of the membrane in the radial direction. In particular, the maximum diplacement is observed at the membrane tip, where contact occurs with the pump flange, without exiting from the pump domain (as discussed in Sect. 3.2).

Finally, we computed the solid Von Mises stress in the wave membrane to study the material resistance at different frequencies of oscillation. In particular, in Figure 11 we showed this quantity for operating point F3 at time $t = 0.052$ s and its maximum and volumetric mean values for each tested frequency. We can observe that the solid stress increased with the frequency of oscillation and that the maximum was achieved at the junction with the membrane holder (gray region) during the ascending phase of the membrane holder.

3.4 Hemocompatibility analysis

Hemocompatibility-related adverse events in WMBPs, such as hemolysis or thrombosis, are closely related to hemodynamic-generated stress exerted on blood cells [15]. In Figure 12, left, we reported for F3 the fluid shear stress σ^{scalar} defined in Eq. (3) in the pump head, where the highest values of stresses are observed, especially on the pump head flanges, nearby the tip of the membrane, where the structure velocity is maximum and where the membrane approaches closely to the wall. In particular, the decomposition of the shear stress tensor highlighted that, unlike in the most part of the pump volume, the hydrostatic component dominates over the deviatoric part in the contact regions, indicating that blood cells in the interstitial fluid are more compressed than distorted by the wave membrane.

In Figure 12, right, we showed the time evolution of the volumetric mean of σ^{scalar} in the pump head during the last period of oscillation, for all operating points. Notice that the fluid stresses increase for larger values of Φ and f, whereas, they decrease for increasing ΔP. The trend of σ^{scalar} is similar for all operating points, showing a peak at π, when membrane holder velocity is maximum.

In order to assess the potential of inducing inside-pump hemolysis and thrombosis, we reported in Table 5 the statistics of σ^{scalar} for all operating points. In particular: the 'Max' column corresponds to the highest value of σ^{scalar} during the last period of oscillation; the 'Mean' column refers to the maximum-in-time of the volumetric mean of σ^{scalar} in the pump head region; the volume percentages indicate the portions of pump volume with σ^{scalar} lowering thresholds of 0.1 Pa and 1 Pa, values that are representative of very low and low stress regions, respectively, or exceeding typical thresholds for hemocompatibility, i.e. 9 Pa indicating the activation of Von Willebrand factor [16], and 50 Pa for platelets activation [21].

Notice that all operating points show low stress conditions, with most of the pump volume (65-75%) with fluid stress smaller than 1 Pa and no occurrence of values exceeding 50 Pa. As a consequence, in our simulations WMBPs showed very low potential for shear-induced platelet activation or hemolysis, which are hypothesized to occur at shear stress conditions over 50 and 150 Pa, respectively [16, 23] .

OP	σ^{scalar} [Pa]		Volume percentage [%] with σ^{scalar}			
	Max	Mean	< 0.1 Pa	< 1 Pa	> 9 Pa	> 50 Pa
P1	39.0	3.26	13.4	74.2	0.09	0
P2/F1	22.8	2.98	10.1	73.5	0.03	0
F2/S1	24.2	3.40	7.8	71.3	0.09	0
F3	27.0	4.06	5.9	66.3	0.25	0
S2	25.1	3.66	6.6	69.2	0.16	0
S3	29.1	3.9	5.8	67.2	0.22	0

Table 5: Stress statistics for each operating point.

3.5 Nominal operating conditions

The primary ambition of the WMBP system is to provide a physiological pulsatile flow to patients suffering of advanced heart failure. Therefore, the pump hydraulic and hemocompatibility performance should be studied over the entire heart cycle, with the head pressure ΔP varying in time. Here, for computational reasons, we limit the analysis to a fixed operating condition to initiate the process of prediction of pump performance using numerical models. In particular, we chose to study a typical operating condition (here refered to *nominal operating point*, NOP) generating physiologic mean flow at head pressure $\Delta P = 80$ mmHg, with oscillation parameters $f = 60$ Hz and $\Phi = 1.8$ mm. This value of head pressure corresponds to the standard pressure difference between systemic and left ventricular pressure at diastole in a failed heart with LVAD support [26].

The pump system was simulated for $T = 0.05$ s, corresponding to three periods of oscillation, using a fixed timestep $\Delta t = 0.0002$ s, with contact parameters $\varepsilon_c = 0.2$ mm and $\gamma_c = 0.2$. Notice that the contact parameters have been increased with respect to default values in Section 3, because of the larger membrane undulations observed during the simulations, probably due to the higher stroke parameter. The physical parameters are set as in Section 3.3.

Figure 13 shows the trend in time of Q (left) and the membrane envelope at NOP. The time-averaged LVAD output amounts to 6.25 $^{L}/_{min}$. In addition, maximum and volumetric mean of σ^{scalar} are plotted in time during the last period of oscillation (Figure 14a). The maximum value is 56.4 Pa, while the volumetric mean in the pump head reaches a maximum of 5.3 Pa at time $t = 0.0432$ s, i.e. during the descending phase of the membrane holder. The volumetric distribution of the *elemental shear stress*, i.e. the average value of σ^{scalar} in each element, is represented in the histogram in Figure 14b. This analysis highlights that stress values above 20 Pa are overall limited to less than 1 mm^3 in the pump volume.

4 Discussion

Wave membrane blood pumps, developed at CorWave SA, are a new family of cardiac assist devices based on an innovative technology where the propulsion of blood is obtained by the undulations of an immersed elastic membrane. This was introduced mainly to try to overcome the limitations of standard rotor-based LVADs, in particular to provide a pulsatile flow rate to the body and to reduce the risk of hemocompatibility-related adverse events. We believe that the research on this new pump and the study of the influence of its design and operating points on its performance could be of interest for the bioingeneering and medical community.

For such reasons, in this work we have presented a computational study of a new design of WMBP (J-shape membrane pump) and compared its performance with that of a previously studied pump (flat membrane pump) [24].

Our numerical results, in good agreement with the experimental findings (see Figure 8, right), showed a drastic increase in the hydraulic performance of the J-shape design with respect to the flat one. Such improvement could be ascribed mainly to the curved and elongated membrane geometry that allowed to separate the flow across the two sides of the membrane holder, reducing flow recirculations around the magnet, which causes hydraulic energy dissipation, differently from what was found for the flat design pump (see Figure 6 in [24]). At identical operating conditions, the increase in the flow conditions led to higher shear rate conditions, which were however still significantly lower than the critical threshold of 42000 s^{-1} [4].

The J-shape design produced the same hydraulic output of the flat one at lower oscillation frequencies ($44 - 60\,Hz$ vs $120\,Hz$) with a beneficial effect on the pump hemocompatibility (lower fluid shear stress) and an increase fatigue life of the membrane (lower solid Von Mises stress).

In our numerical results, we observed that the pump output increased of 0.35-0.45 $^{L}/_{min}$, for every increment of 5 Hz of oscillation frequency, while it increased by 0.6-0.7 $^{L}/_{min}$, when the stroke is increased by 0.1 mm. These data can then be used to further refine and optimize the membrane design and performance, in view of future in-human trials. In particular, we tested the nominal operating point, with higher membrane oscillation parameters ($f = 60$ Hz, $\Phi = 1.8$ mm), that allowed to recover physiological output ($\simeq 5/6\,L/min$) at $\Delta P = 80$ mmHg, thanks to a better isolation of the fluid pockets during their transport in the pump head. Nonetheless, the operating point should be tested also at different head pressures to fully characterize the HQ trend and capture the global behavior of the pulsatile pump. With the aim of reducing the computational time and explore several scenarios, some studies considered lumped parameter models to rapidly provide qualitative information of the pump performance over the heart cycle for variable head pressure [37].

Another new contribution of the present work was the introduction of a contact model to handle at the numerical level the recurring impingement between

the membrane and the pump flanges at high oscillations. Indeed, we considered here more realistic operating conditions of the membrane than what seen in [24], with an increase in stroke of $40\% - 70\%$, that allowed for a more effective transport of the fluid pockets towards the outlet without backflow, but lead to contact between membrane and flanges. We also identified suitable ranges for the contact parameters ε_c and γ_c, that allow to obtain a contact force that prohibits non-physical membrane penetration out from the pump boundary (see Figure 7), without affecting significantly wave propagation and pump outflow.

Finally, we want to discuss the hemocompatibility of the new pump. In LVADs blood shear stresses are considered to be good indicators of the risk of hemocompatibility-related adverse events. In particular, large fluid shear stress peak values, e.g. above 150 Pa [16, 23], are frequently markers for hemolysis potential, especially in case of long exposure time. In our simulations, we observed reduced levels of such quantity, with most of the pump volume (65%-75%) presenting values below 1 Pa and a maximum value for the NOP equal to 56.4 Pa, significantly lower than the critical threshold. Other studies indicated that lower shear stress thresholds could be significant from the point of view of thrombogenesis: for instance, Von Willebrand factor protein, that mediates the platelet adhesion, is activated at fluid stress levels higher than 9 Pa [16], while platelets are activated at shear stress higher than 50 Pa [21]. Both these thresholds are very rarely achieved in our pump, and only locally in space and time, see Table 5. Low fluid shear stress conditions should also be avoided, because they increase the likelihood of platelets deposition and aggregation, that can lead to thrombosis [35]. In our numerical results, only 5-15% of the pump volume presents very low shear stress values (smaller than 0.1 Pa), especially when the frequency of oscillation is low.

Some limitations characterized this study. First, we omitted from the computational domain a set of thin suspension springs that are employed to maintain the magnet ring centered around the actuator. Their inclusion may deform the flow patterns near the magnet ring. Second, the membrane holder, that is actually a separate component embedded in the elastic membrane, is here modeled as part of the membrane assembly, as done in [24]. In principle, this simplification may affect the membrane displacement close to the junction of the membrane holder. Third, although we observed strains smaller than 10%, the assumption of linear elasticity for the membrane could be improved in future works by considering a finite elasticity model to better describe the membrane dynamics and its interaction with blood. Finally, we observe that we have used fluid-dynamics quantities (such as shear stresses) to obtain preliminary results about hemocompatibilty. Although shear stresses provide significant indications in such a direction as highlighted by several works [16, 16, 21, 23, 35], more direct analyses provided by the introduction of an hemolysis model could be developed for future works to properly assess the risk of hemolysis and estimate the mean residence time in WMBP.

Acknowledgements

This project has received funding from the European Union's Horizon 2020 research and innovation programme under the Marie Skłodowska-Curie grant agreement "ROMSOC - Reduced Order Modelling, Simulation and Optimization of Coupled systems" - No 765374. MM and CV are members of the INdAM Research group GNCS. The authors wish to acknowledge Charlotte Rasser from CorWave SA for her assistance in manuscript editing and revision.

References

[1] F. Alauzet, B. Fabrèges, M. A. Fernández, and M. Landajuela. Nitsche-XFEM for the coupling of an incompressible fluid with immersed thin-walled structures. *Computer Methods in Applied Mechanics and Engineering*, 301:300–335, 2016.

[2] A. C. Alba and D. H. Delgado. The future is here: Ventricular Assist Devices for the failing heart. *Expert Review of Cardiovascular Therapy*, 7(9):1067–1077, 2009.

[3] Larry A Allen, Colleen K McIlvennan, Jocelyn S Thompson, Shannon M Dunlay, Shane J LaRue, Eldrin F Lewis, Chetan B Patel, Laura Blue, Diane L Fairclough, Erin C Leister, et al. Effectiveness of an intervention supporting shared decision making for destination therapy left ventricular assist device: the DECIDE-LVAD randomized clinical trial. *JAMA internal medicine*, 178(4):520–529, 2018.

[4] D. Arora, M. Behr, and M. Pasquali. Hemolysis estimation in a centrifugal blood pump using a tensor-based measure. *Artificial organs*, 30(7):539–547, 2006.

[5] C. Bartoli and R. Dowling. The next wave of Mechanical Circulatory Support Devices. *Cardiac Interventions Today*, 13(1):53–59, 2019.

[6] M. Behbahani, M. Behr, M. Hormes, U. Steinseifer, D. Arora, O. Coronado, and M. Pasquali. A review of computational fluid dynamics analysis of blood pumps. *European Journal of Applied Mathematics*, 20(4):363–397, 2009.

[7] L. Bertagna, S. Deparis, L. Formaggia, D. Forti, and A. Veneziani. The LifeV library: engineering mathematics beyond the proof of concept. *arXiv preprint arXiv:1710.06596*, 2017.

[8] C Bludszuweit. Three-dimensional numerical prediction of stress loading of blood particles in a centrifugal pump. *Artificial Organs*, 19(7):590–596, 1995.

[9] Danny Bluestein. Research approaches for studying flow-induced thromboembolic complications in blood recirculating devices. *Expert review of medical devices*, 1(1):65–80, 2004.

[10] J. Bonnemain, A. C. I. Malossi, M. Lesinigo, S. Deparis, A. Quarteroni, and L. K. Von Segesser. Numerical simulation of left ventricular assist device implantations: comparing the ascending and the descending aorta cannulations. *Medical engineering & physics*, 35(10):1465–1475, 2013.

[11] Carl Botterbusch, Trevor Snyder, Pier-Paolo Monticone, Louis de Lillers, Alexandra Schmidt, and Charlotte Rasser. CorWave LVAD: Insight into device concept and stage of development. In *Mechanical Support for Heart Failure*, pages 587–597. Springer, 2020.

[12] Erik Burman, Miguel A Fernández, and Stefan Frei. A Nitsche-based formulation for fluid-structure interactions with contact. *ESAIM: Mathematical Modelling and Numerical Analysis*, 54(2):531–564, 2020.

[13] Anamika Chatterjee, Silvia Mariani, Jasmin S Hanke, Tong Li, Ali Saad Merzah, Regina Wendl, Axel Haverich, Jan D Schmitto, and Günes Dogan. Minimally invasive left ventricular assist device implantation: optimizing device design for this approach. *Expert review of medical devices*, 17(4):323–330, 2020.

[14] Corstiaan A Den Uil, Sakir Akin, Lucia S Jewbali, Dinis dos Reis Miranda, Jasper J Brugts, Alina A Constantinescu, Arie Pieter Kappetein, and Kadir Caliskan. Short-term mechanical circulatory support as a bridge to durable left ventricular assist device implantation in refractory cardiogenic shock: a systematic review and meta-analysis. *European Journal of Cardio-Thoracic Surgery*, 52(1):14–25, 2017.

[15] K. H. Fraser, M. E. Taskin, T. Zhang, B. P. Griffith, and Z. J. Wu. Comparison of shear stress, residence time and lagrangian estimates of hemolysis in different ventricular assist devices. In *26th Southern Biomedical Engineering Conference SBEC 2010, April 30-May 2, 2010, College Park, Maryland, USA*, pages 548–551. Springer, 2010.

[16] Katharine H Fraser, Tao Zhang, M Ertan Taskin, Bartley P Griffith, and Zhongjun J Wu. A quantitative comparison of mechanical blood damage parameters in rotary ventricular assist devices: shear stress, exposure time and hemolysis index. *Journal of biomechanical engineering*, 134(8):081002, 2012.

[17] A. Gerstenberger and W. A. Wall. An extended finite element method/Lagrange multiplier based approach for fluid–structure interaction. *Computer Methods in Applied Mechanics and Engineering*, 197(19-20):1699–1714, 2008.

[18] Christophe Geuzaine and Jean-François Remacle. Gmsh: A 3-D finite element mesh generator with built-in pre-and post-processing facilities. *International journal for numerical methods in engineering*, 79(11):1309–1331, 2009.

[19] Roland Graefe, Andreas Henseler, Reiner Körfer, Bart Meyns, and Libera Fresiello. Influence of left ventricular assist device pressure-flow characteristic on exercise physiology: Assessment with a verified numerical model. *The International journal of artificial organs*, 42(9):490–499, 2019.

[20] A. Hansbo and P. Hansbo. An unfitted finite element method, based on Nitsche's method, for elliptic interface problems. *Computer methods in applied mechanics and engineering*, 191(47-48):5537–5552, 2002.

[21] J David Hellums. 1993 Whitaker Lecture: biorheology in thrombosis research. *Annals of biomedical engineering*, 22(5):445–455, 1994.

[22] Sagar Kadakia, Ryan Moore, Vishnu Ambur, and Yoshiya Toyoda. Current status of the implantable LVAD. *General thoracic and cardiovascular surgery*, 64(9):501–508, 2016.

[23] V. Kannojiya, A. K. Das, and P. K. Das. Numerical simulation of centrifugal and hemodynamically levitated LVAD for performance improvement. *Artificial Organs*, 44(2):E1–E19, 2019.

[24] Marco Martinolli, Jacopo Biasetti, Stefano Zonca, Luc Polverelli, and Christian Vergara. Extended finite element method for fluid-structure interaction in wave membrane blood pump. *International Journal for Numerical Methods in Biomedical Engineering*, page e3467, 2021.

[25] U. M. Mayer, A. Popp, A. Gerstenberger, and W. A. Wall. 3D fluid–structure-contact interaction based on a combined XFEM FSI and dual mortar contact approach. *Computational Mechanics*, 46(1):53–67, 2010.

[26] N. Moazami, K. Fukamachi, M. Kobayashi, N. G. Smedira, K. J. Hoercher, A. Massiello, S. Lee, D. J. Horvath, and R. C. Starling. Axial and centrifugal continuous-flow rotary pumps: a translation from pump mechanics to clinical practice. *The Journal of heart and lung transplantation*, 32(1):1–11, 2013.

[27] A. Molteni, Z. P. H. Masri, K. W. Q. Low, H. N. Yousef, J. Sienz, and K. H. Fraser. Experimental measurement and numerical modelling of dye washout for investigation of blood residence time in ventricular assist devices. *The International journal of artificial organs*, 41(4):201–212, 2018.

[28] Christos A Papanastasiou, Konstantinos G Kyriakoulis, Christina A Theochari, Damianos G Kokkinidis, Theodoros D Karamitsos, and Leonidas

Palaiodimos. Comprehensive review of hemolysis in ventricular assist devices. *World Journal of Cardiology*, 12(7):334–341, 2020.

[29] L. Pauli, J. Nam, M. Pasquali, and M. Behr. Transient stress-based and strain-based hemolysis estimation in a simplified blood pump. *International journal for numerical methods in biomedical engineering*, 29(10):1148–1160, 2013.

[30] M. Perschall, J. B. Drevet, T. Schenkel, and H. Oertel. The progressive wave pump: numerical multiphysics investigation of a novel pump concept with potential to ventricular assist device application. *Artificial organs*, 9(36):E179–E190, 2012.

[31] A. Quarteroni, L. Dedè, A. Manzoni, and C. Vergara. *Mathematical Modelling of the Human Cardiovascular System - Data, Numerical Approximation, Clinical Applications*. Cambridge University Press, 2019.

[32] M. Scheffler, N. Mechbal, E. Monteiro, M. Rebillat, and R. Pruvost. Implementation and evaluation of a sensorless, nonlinear stroke controller for an implantable, undulating membrane blood pump. *IFAC-PapersOnLine*, 53(2):8683–8688, 2020.

[33] B. Thamsen, B. Blümel, J. Schaller, C. O. Paschereit, K. Affeld, L. Goubergrits, and U. Kertzscher. Numerical analysis of blood damage potential of the HeartMate II and HeartWare HVAD rotary blood pumps. *Artificial organs*, 39(8):651–659, 2015.

[34] Christina A Theochari, George Michalopoulos, Evangelos K Oikonomou, Stefanos Giannopoulos, Ilias P Doulamis, M Alvarez Villela, and Damianos G Kokkinidis. Heart transplantation versus left ventricular assist devices as destination therapy or bridge to transplantation for 1-year mortality: a systematic review and meta-analysis. *Annals of cardiothoracic surgery*, 7(1):3–11, 2018.

[35] S. R. Topper, M. A. Navitsky, R. B. Medvitz, E. G. Paterson, C. A. Siedlecki, M. J. Slattery, S. Deutsch, G. Rosenberg, and K. B. Manning. The use of fluid mechanics to predict regions of microscopic thrombus formation in pulsatile VADs. *Cardiovascular engineering and technology*, 5(1):54–69, 2014.

[36] S S Virani, Alvaro Alonso, Emelia J Benjamin, Marcio S Bittencourt, Clifton W Callaway, April P Carson, Alanna M Chamberlain, Alexander R Chang, Susan Cheng, Francesca N Delling, et al. Heart disease and stroke statistics - 2020 update: a report from the American Heart Association. *Circulation*, 141(9):e139–e596, 2020.

[37] Yiwen Wang, Peng Shen, Minli Zheng, Pengqiang Fu, Lijia Liu, Jingyue Wang, and Lishan Yuan. Influence of impeller speed patterns on hemodynamic characteristics and hemolysis of the blood pump. *Applied Sciences*, 9(21):4689, 2019.

[38] Ashleigh Xie, Kevin Phan, and Tristan D Yan. Durability of continuous-flow left ventricular assist devices: a systematic review. *Annals of cardiothoracic surgery*, 3(6):54756–54556, 2014.

[39] S. Zonca, C. Vergara, and L. Formaggia. An unfitted formulation for the interaction of an incompressible fluid with a thick structure via an XFEM/DG approach. *SIAM Journal on Scientific Computing*, 40(1):B59–B84, 2018.

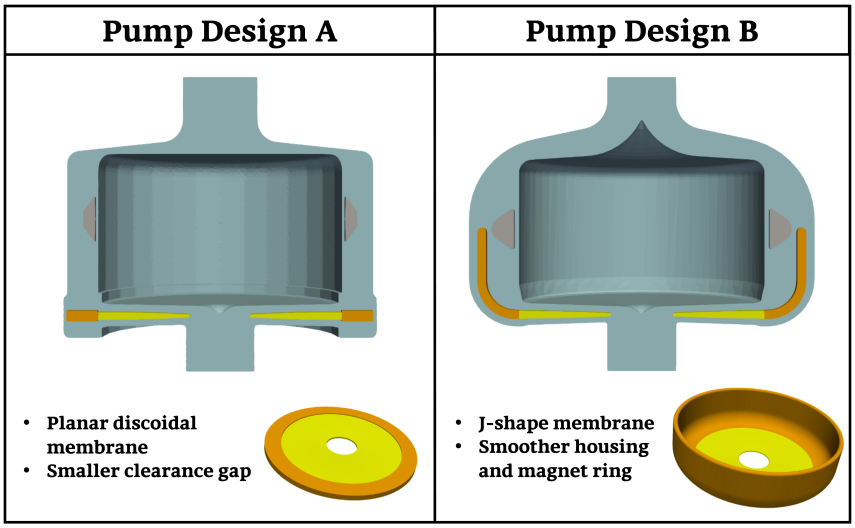

Figure 2: Comparison of flat membrane pump design (A) and J-shape membrane pump design (B), with focus on the different geometries of the membrane holder (orange).

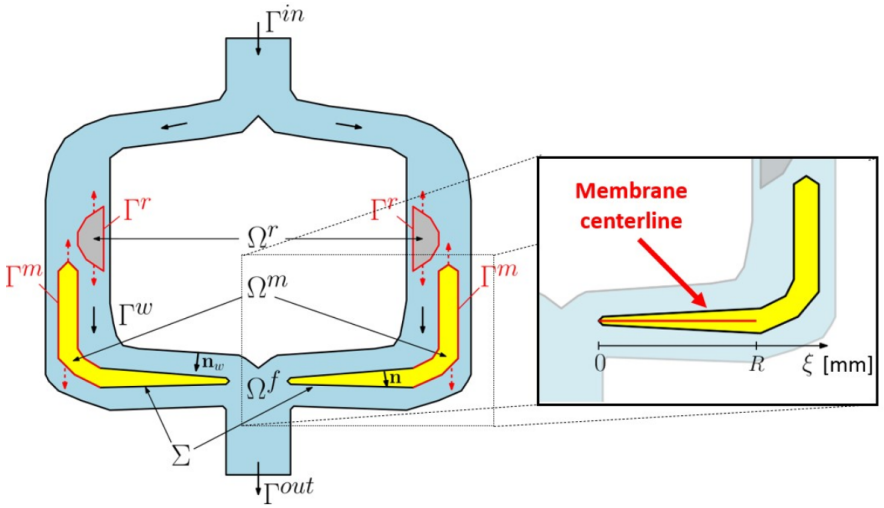

Figure 3: Left: Cross-section of the wave membrane blood pump domain: fluid domain Ω^f (cyan), membrane domain Ω^m (yellow), magnet ring Ω^r (gray). Γ^{in} and Γ^{out} are the inlet and the outlet boundaries, and Γ^w is the wall surfaces. Γ^m and Γ^r (red) are the boundaries of the membrane holder and of the magnetic ring, respectively, where the oscillation is imposed by the actuator; Σ is the fluid-structure interface. Right: Zoom on membrane cross-section, with membrane centerline (red) and associated radial coordinate ξ. The length R indicates the radius of the wave deformable membrane.

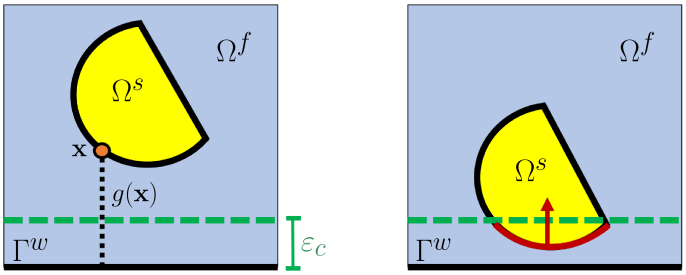

Figure 4: Schematic FSI domains for the relaxed contact model. As the structure Ω^m penetrates into the contact layer (delimited by the green line), whose width is ε_c (left), it receives a repulsive force χ (in red, right).

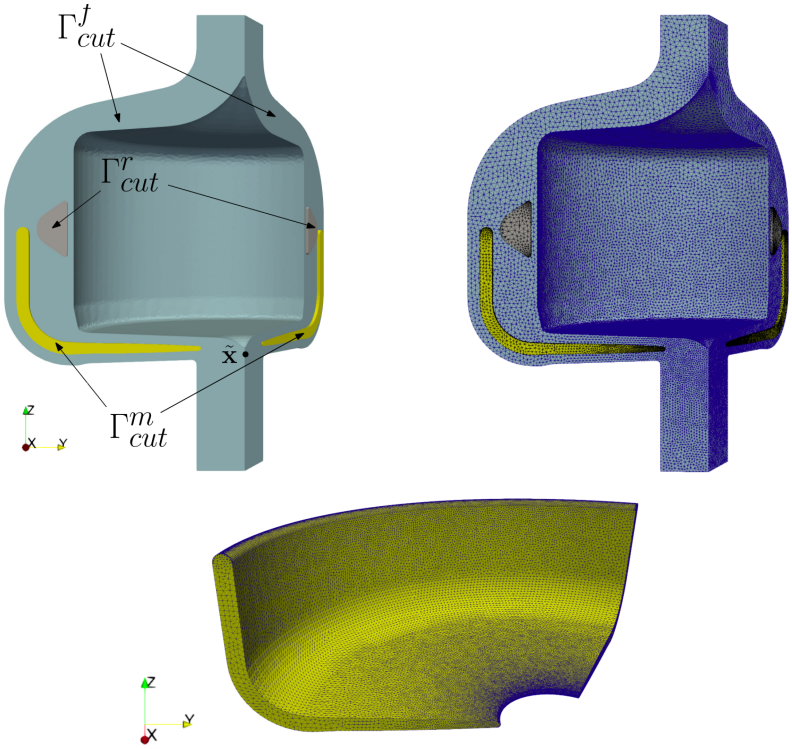

Figure 5: Left: Reduced geometry limited to a 120-degree pump section. Γ^f_{cut}, Γ^m_{cut} and Γ^r_{cut} are the artificial sections of each domain, generated by the vertical cuts of the full axi-symmetric geometry. Point $\tilde{\mathbf{x}}$ denotes the point used for the grid convergence analysis. Right: Visualization of the fluid, membrane and magnet ring meshes. Below: Membrane mesh.

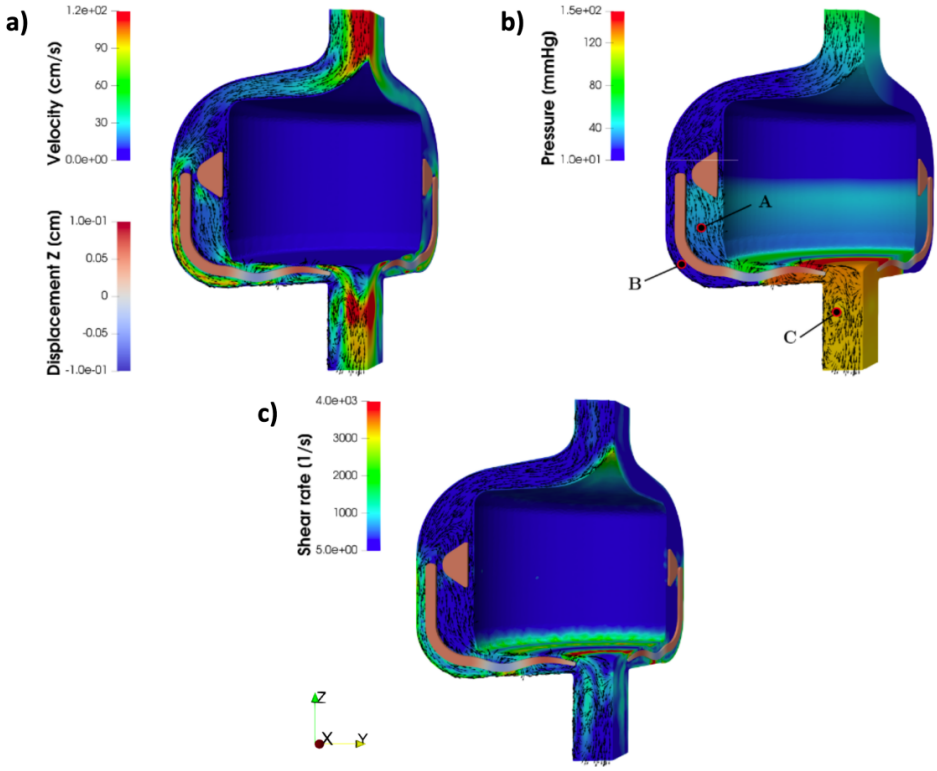

Figure 6: Visualization of blood velocity (a), pressure (b), and shear rate (c) fields at time $t = 0.0188$ s (maximum membrane oscillation), for HF1 operating point ($\Delta P = 50$ mmHg).

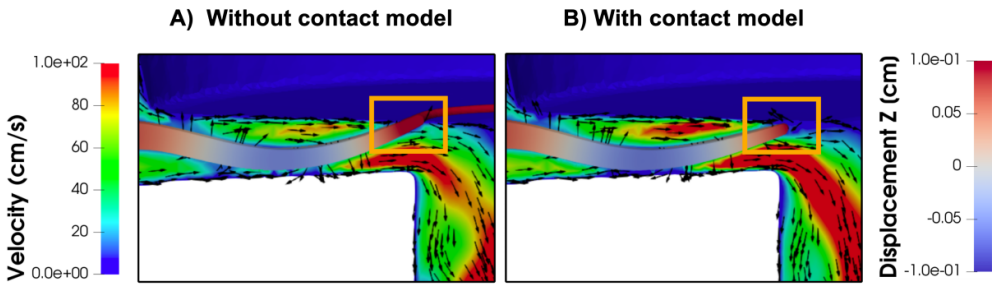

Figure 7: Snapshot of numerical simulation without (A) and with contact model (B) at time $t = 0.044$ s. The orange box identifies the region of highest membrane deformation, that causes the exit of the membrane from the pump fluid domain when no contact model is considered.

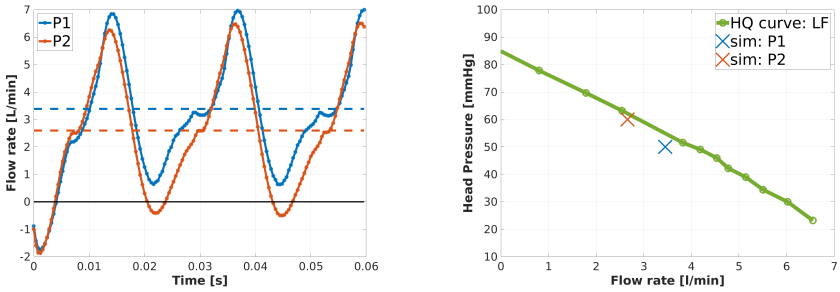

Figure 8: Outlet flow rate in time (left) and comparison between experimental HQ curves (line) and numerical results (crosses, right). P-analysis.

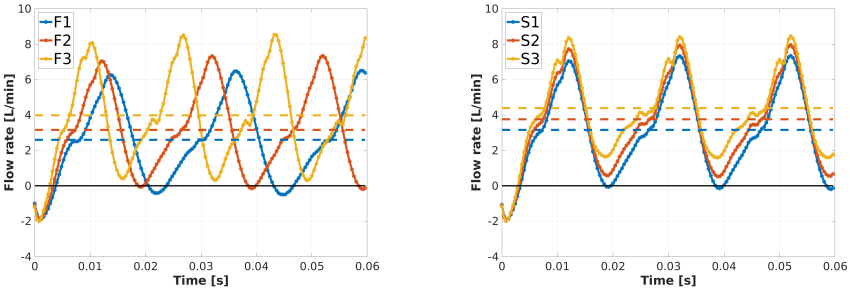

Figure 9: Time evolution of the flow rate at the outlet for different values of frequency (F-analysis, left) and stroke (S-analysis, right).

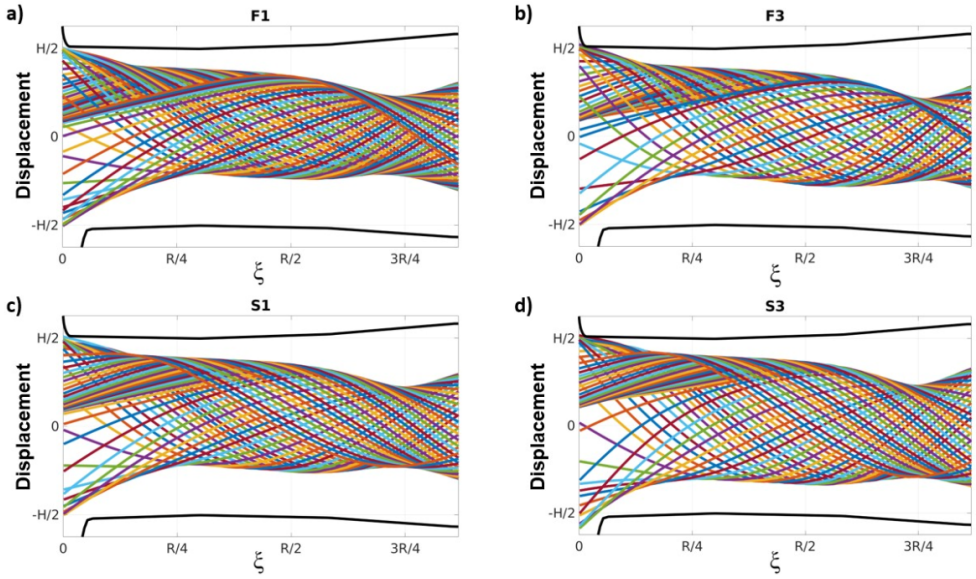

Figure 10: Membrane envelopes for different operating points of the device, at fixed head pressure $\Delta P = 60$ mmHg. The black lines represent the pump head flanges. Membrane radius R and pump head height H are protected for confidentiality.

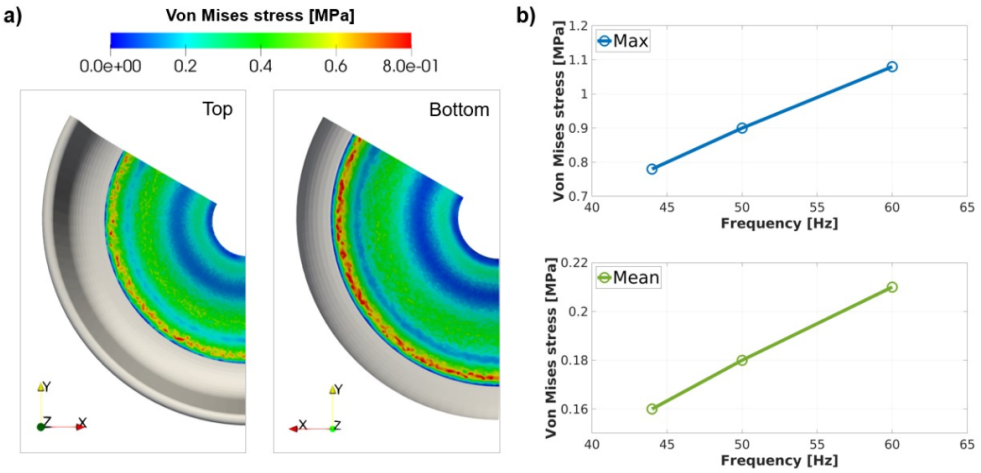

Figure 11: Von Mises stress analysis in the wave membrane. a) Visualization of the Von Mises stress on the top and the bottom surfaces of the wave membrane at time $t = 0.052$ (ascending phase). b) Plots of the maximum (above) and volumetric mean (bottom) Von Mises stress for F1, F2 and F3.

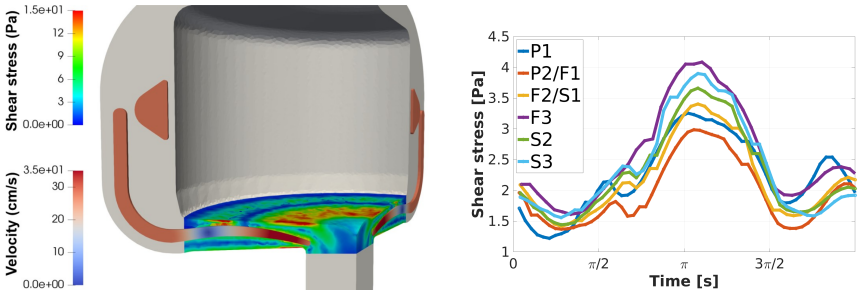

Figure 12: Left: Representation of the fluid shear rate σ^{scalar} at time $t = 0.0568$ s for F3 in the pump head. Right: Time evolution of the volumetric mean of σ^{scalar} in the pump head for different operating points during the last period of oscillation, properly rescaled in the interval $[0, 2\pi]$.

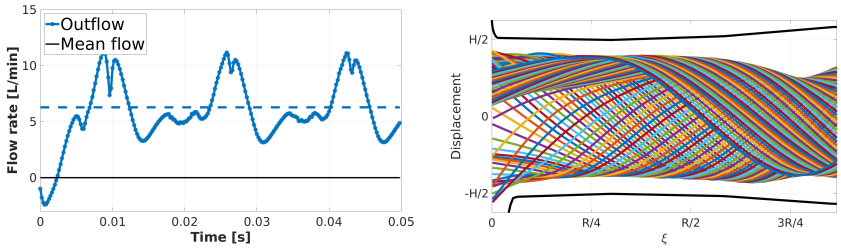

Figure 13: Time evolution of the flow rate at the outlet (left) and visualization of the membrane envelope (right) at nominal operating conditions.

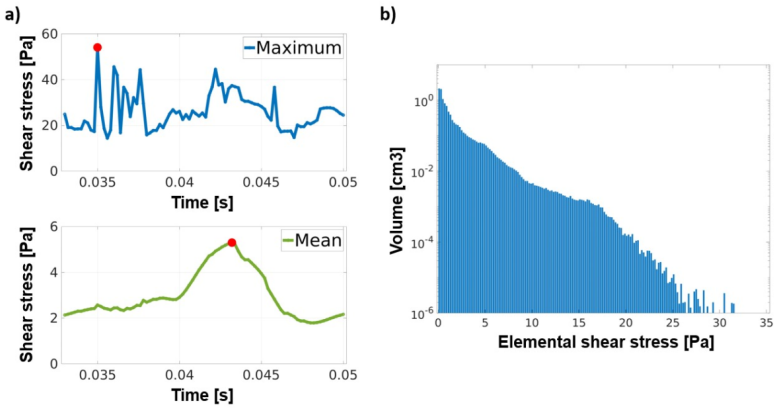

Figure 14: a) Time plot of maximum value (left) and volumetric mean in the pump head (right) of Von Mises stress analysis at nominal operating conditions. Red dot indicates maximum point in time. b) Histogram of volumetric stress for NOP.

MOX Technical Reports, last issues

Dipartimento di Matematica
Politecnico di Milano, Via Bonardi 9 - 20133 Milano (Italy)

39/2021 Barnafi, N.; Di Gregorio, S.; Dede', L.; Zunino, P.; Vergara, C.; Quarteroni, A.
A multiscale poromechanics model integratingmyocardial perfusion and systemic circulation

38/2021 Giusteri, G. G.; Miglio, E.; Parolini, N.; Penati, M.; Zambetti, R.
Simulation of viscoelastic Cosserat rods based on the geometrically exact dynamics of special Euclidean strands

36/2021 Parolini, N.; Dede', L; Antonietti, P. F.; Ardenghi, G.; Manzoni, A.; Miglio, E.; Pugliese, A.; V
SUIHTER: A new mathematical model for COVID-19. Application to the analysis of the second epidemic outbreak in Italy

37/2021 Dassi, F.; Fumagalli, A.; Mazzieri, I.; Scotti, A.; Vacca, G.
A Virtual Element Method for the wave equation on curved edges in two dimensions

34/2021 Bonaventura, L.; Gatti F.; Menafoglio A.; Rossi D.; Brambilla D.; Papini M.; Longoni L.
An efficient and robust soil erosion model at the basin scale

35/2021 Regazzoni, F.; Quarteroni, A.
Accelerating the convergence to a limit cycle in 3D cardiac electromechanical simulations through a data-driven 0D emulator

33/2021 Lupo Pasini, M.; Gabbi, V.; Yin, J.; Perotto, S.; Laanait, N.
Scalable balanced training of conditional generative adversarial neural networks on image data

32/2021 Sangalli, L.M.
Spatial regression with partial differential equation regularization

31/2021 Ferraccioli, F.; Arnone, E.; Finos, L.; Ramsay, J.O.; Sangalli, L.M.
Nonparametric density estimation over complicated domains

30/2021 Fumagalli, I.
A reduced 3D-0D FSI model of the aortic valve including leaflets curvature